Seasonal Variations in Mercury's Dayside Calcium Exosphere

Matthew H. Burger[a], Rosemary M. Killen[b], William E. McClintock[c], Aimee W. Merkel[c], Ronald J. Vervack, Jr.[d], Timothy A. Cassidy[c], Menelaos Sarantos[e]

[a] *Goddard Earth Sciences, Technology, and Research, Morgan State University, Baltimore, MD 21251, USA.*
[b] *Solar System Exploration Division, NASA Goddard Space Flight Center, Greenbelt, MD 20771, USA.*
[c] *Laboratory for Atmospheric and Space Physics, University of Colorado, Boulder, CO 80309, USA.*
[d] *The Johns Hopkins University Applied Physics Laboratory, Laurel, MD 20723, USA.*
[e] *Goddard Planetary Heliophysics Institute, University of Maryland Baltimore County, Baltimore, MD, 21228, USA.*

Abstract

The Mercury Atmospheric and Surface Composition Spectrometer on the MESSENGER spacecraft has observed calcium emission in Mercury's exosphere on a near-daily basis since March 2011. During MESSENGER's primary and first extended missions (March 2011 – March 2013) the dayside calcium exosphere was measured over eight Mercury years. We have simulated these data with a Monte Carlo model of exospheric source processes to show that (a) there is a persistent source of energetic calcium located in the dawn equatorial region, (b) there is a seasonal dependence in the calcium source rate, and (c) there are no obvious year-to-year variations in the near-surface dayside calcium exosphere. Although the precise mecha-

Email address: Matthew.Burger@nasa.gov (Matthew H. Burger)

nism responsible for ejecting the calcium has not yet been determined, the most likely process is the dissociation of Ca-bearing molecules produced in micrometeoroid impact plumes to form energetic, escaping calcium atoms.
Keywords: Mercury; Mercury, atmosphere; Spectroscopy; Atmospheres, structure

1. Introduction

Mercury is surrounded by a surface-bounded exosphere (an atmosphere that is collisionless down to the planet's surface) known to contain both volatile and refractory species derived from the regolith, interplanetary dust, and the solar wind (Killen et al., 2007). The calcium (Ca) component of Mercury's exosphere was first detected from the ground (Bida et al., 2000; Killen et al., 2005), but the MErcury Surface, Space ENvironment, GEochemistry, and Ranging (MESSENGER) spacecraft, in orbit around Mercury since March 2011, has provided the first opportunity for a detailed study of the distribution and variability of calcium near Mercury. Exospheric emissions at Mercury are measured by the Ultraviolet and Visible Spectrometer (UVVS), one component of the Mercury Atmospheric and Surface Composition Spectrometer (MASCS) (McClintock and Lankton, 2007). Calcium emissions are observed on a near-daily basis at 422.7 nm wavelength.

Burger et al. (2012) analyzed UVVS observations of exospheric calcium made prior to orbit insertion and during the first week of science operations. They concluded that all the calcium detected could be supplied by an energetic source (characterized by a temperature $T \gtrsim$20,000 K if the source flux has a Maxwellian distribution) centered on or near equatorial dawn. The

physical mechanism producing this calcium distribution was not evident, but Burger et al. (2012) concluded that the distribution did not appear to be related to either magnetospheric effects or material that had built up on the nightside and desorbed as it rotated into sunlight. In this study, we extend the work of Burger et al. (2012) using data from MESSENGER's primary and first extended missions spanning eight Mercury years.

2. UVVS observations of dayside calcium

Designed to detect exospheric emission around Mercury, the UVVS feeds observations from a telescope to a grating monochromator that scans a series of narrow wavelength ranges centered on the resonance lines of expected atomic species (McClintock and Lankton, 2007). Each Ca spectral scan is centered on the Ca emission line center (422.7 nm) and covers a wavelength range of 421.1–424.4 nm with a 0.2 nm step size. Doppler shifts of the line center due to different radial velocities of MESSENGER and Mercury are on the order of 0.017 nm and are negligible with a 0.5 nm instrument passband. The signal detected by the instrument is a combination of Ca emission, solar light scattered from Mercury's dayside surface, and a detector dark offset. The solar contribution is light reflected from Mercury's surface that is scattered into the monchromator entrance slit by the telescope mirrors, and a correction is determined from the observations. The dark offset arises from thermionic emission within the detector and is a function of instrument temperature. The dark offset is fully characterized through routinely sampled measurements on the nightside of the planet.

Two Ca spectral scans taken on MESSENGER orbit 905, one near the dawn terminator and one near the dusk terminator, are illustrated in Fig-

ure 1. To retrieve the Ca emission component of the scan, the solar background must be estimated and removed. The solar scattering component (red line) is determined by fitting a solar continuum spectrum to the dark-subtracted spectral scan (black line) using the wavelengths near the ends of the scans that do not contain exosphere emission (shown in green). Scaling the solar continuum to the wings of the measured spectral scan maintains the core-to-wing ratio of the Fraunhofer feature in the solar spectrum (at 422.7 nm) and provides an accurate estimate of the solar background. The dark and scattered sunlight components of the spectral scans are subtracted from the measured signal, and the residual is assumed to be Ca emission from the exosphere. The instrument radiometric sensitivity calibration is applied to convert from counts per second to radiance (Fig. 1c and 1d), and the five points around line center are summed to obtain a total Ca radiance value in kilorayleighs (kR) for each spectral scan. The totals for the given examples are 13.0 kR and 1.2 kR, respectively.

Observing the Ca emission near Mercury's surface is a challenge because there is a large solar scattering component to remove. This challenge is evident in the difference between the two spectral scans shown in Fig. 1. Both spectral scans were taken on orbit 905 at a tangent altitude of 220 km, but at two different local times. The viewing geometry with respect to Mercury's surface is very similar in both examples. The scan shown in Fig. 1a was taken near the dawn terminator where the abundance of Ca is high, and its emission dominates the solar scattering component. The scan shown in Fig. 1b, in contrast, was taken near the dusk terminator where the Ca abundance is much lower and the solar scattering component dominates the signal. Dom-

inance by the solar scattering component increases the uncertainty in the measurements, shown by the signal-to-noise ratio (SNR) of these two examples (36 and 4, respectively). This issue is a limiting factor in our ability to detect Ca when the abundance is small. Only Ca data with a SNR greater than 2 are used for comparison with model simulations.

For this study we have included UVVS observations of Mercury's dayside calcium exosphere from MESSENGER's primary mission (18 March 2011–17 March 2012 orbits 1–738) and first extended mission (18 March 2012–17 March 2013, orbits 739–1804). [The MESSENGER orbits are numbered from apoapsis, with orbit 1 corresponding to the Mercury orbit insertion (MOI) orbit]. The data cover portions of nine Mercury years. By convention of the MESSENGER science team, the Mercury year begins at perihelion [true anomaly angle (TAA) = 0°].

Several observing strategies using UVVS were employed to determine the exospheric structure. To explore the dayside, spectra were acquired during a series of limb scans over several dayside local times. Limb scans were generally obtained when MESSENGER was near apoapsis south of Mercury. UVVS was pointed northward and scanned radially in altitude over the surface at an approximately fixed local time to produce radial profiles of the exospheric emission. The azimuthal structure was obtained by performing multiple limb scans at different local times during a single orbit. The maximum number of scans during an orbit was 13, although the number could be as few as one, depending on the observing circumstances. For the dataset used in this study, there are 465 orbits with at least one limb scan. Table 1 lists the number of orbits with n limb scans, where n is between 1 and 13.

Each spectrum in a limb scan corresponds to a single UVVS line of sight (LOS). A LOS is characterized by its tangent point, i.e., the point at which the line of sight is closest to Mercury's surface. Mercury is assumed to be a perfect sphere with radius $R_{\rm M}$=2440 km. During these limb scans, each LOS is directed approximately south to north, although the precise angle it makes with the equatorial plane depends on the location of the spacecraft in its orbit. Most of the scans are taken when MESSENGER is between 12,000 km and 6000 km from Mercury, and the slit projection changes from 240 km to 120 km. As shown below, the e-folding distances are >1000 km; therefore, there is little variation in the radiance of the exosphere across the slit. Figure 2 shows a typical viewing geometry for dayside limb scans. The endpoints of each LOS in this depiction are the spacecraft and the tangent point. The color indicates the observed radiance ($4\pi I$ measured in kR). The tangent point is uniquely defined by its local time (L) and altitude (A) above the surface. (Lines of sight however are not uniquely determined by L and A because the tangent point can be anywhere along the meridian at L and the angle between the LOS and the equatorial plane can vary.) Limb scans have been obtained only over the dayside at local times between 6 and 18 h (dawn and dusk, respectively).

The limb scan data support the conclusions of Burger et al. (2012) that the Ca source peaks in the dawn region. Figure 3 shows interpolated images of the limb scan data projected onto the equatorial plane. Data from three epochs during the time period under consideration indicate that this dawn enhancement is a persistent feature independent of time and Mercury true anomaly. The images were constructed with a method similar to that used by

McClintock et al. (2008) to make images of the emission from Mercury's anti-sunward tail region. We first computed L and A of the LOS tangent point and interpolated emission measured along these lines of sight onto a regular grid. We then performed a transformation from the polar (A, L) coordinate system to a cartesian (x, y, where the x-axis points towards dusk and the y-axis points away from the Sun) coordinate system to estimate the emission at all points in the dayside equatorial plane as seen from a vantage point above Mercury's north pole. When viewing these reconstructions, it is important to keep in mind that the radial sampling is much better than the azimuthal sampling. Therefore radial variations and large-scale azimuthal structure are real, but small-scale azimuthal structure is an artifact of the relatively poor sampling in local time. We also note that these images are intended only to provide a visual sense of the data. In the analysis that follows, we work with the actual data only and not the interpolated approximations between data points. It is clear, however, that the dawn enhancement in the emission is the dominant morphological feature in the Ca data.

The emission data also indicate that the Ca exosphere is stable from one year to the next. This result was determined by fitting exponential functions to each radial profile:

$$4\pi I(A, L) = 4\pi I_0(L) e^{-A/H} \tag{1}$$

where $4\pi I(A, L)$ is the observed radiance at altitude A and local time L at each tangent point above Mercury's surface, $4\pi I_0(L)$ is the radiance at the surface as a function of local time, and H is the e-folding (e^{-1}) distance. H differs from a true scale height as defined by Chamberlain (1963) due to the high ionization rate. The parameters $4\pi I_0$ and H for fits to limb scans at

dawn are plotted versus Mercury true anomaly in Fig. 4a and 4b. Different Mercury years are indicated by different colors. Little to no year-to-year variability is evident in the data. The primary variation in $4\pi I_0$ (Fig. 4a) is due to the changing g-value, the product of the solar flux at the emission wavelength and the scattering probability per atom. In Fig. 4c we have approximately removed the effect of g-value by converting to the apparent illuminated column density at the surface N_0 using:

$$N_0 = \frac{4\pi I_0}{g} \times 10^9 \tag{2}$$

where $4\pi I_0$ has units of kR and g is the g-value for an atom at rest relative to Mercury in units of photons atom^{-1} s^{-1}, as computed by Killen et al. (2009).

The approximation used in Equation 2 introduces a systematic error owing to the assumption that all the atoms are at rest relative to Mercury so that a constant g-value can be used at each true anomaly. Because exospheric calcium is mostly escaping, this assumption is not valid – the g-values for individual atoms are different from Mercury's g-value. The consequences of this assumption are greatest at perihelion and aphelion because at these true anomalies, Mercury's radial velocity relative to the Sun is zero and its g-value is minimized. Any radial motion that the Ca atoms experience, whether toward or away from the Sun, increases their g-values relative to Mercury such that the actual mean g-value for the atoms is greater than that obtained under the assumption of no radial motion. This therefore creates an apparent peak in N_0 at aphelion and exaggerates the peak at perihelion. At other true anomalies, deviations from Mercury's radial velocity will cancel out if equal numbers of atoms are moving toward and away from Mercury. For Ca, which is ejected energetically and is mostly escaping, the deviations do

not cancel out. At local times near dawn or dusk, where the Ca is moving mostly perpendicular to the Sun-Mercury direction, the column density derived from Equation 2 differs from the actual column density by $\sim 10\%$, but varies with true anomaly. Near the sub-solar point, where the difference in radial velocity relative to the sun between Mercury and exospheric Ca are greatest, the errors introduced by use of Equation 2 are larger, approaching a factor of 2, and have a larger variation over the course of a Mercury year than near the terminator.

In the next section we quantify the seasonal variability (the variation with true anomaly) with a Monte Carlo model that takes into account the motion of atoms relative to Mercury when computing g-values. The above empirical analysis has been presented primarily to show that (a) there appears to be a seasonal variation in the Ca source at dawn, and (b) the Ca source appears to have no year-to-year variability. In our models of the limb scan data presented below, we take advantage of the annual repeatability of the exosphere to increase the local time coverage and number of data points available by binning data from different Mercury years by true anomaly. We note that the dawn brightness asymmetry seen in Figure 3 is not a result of the systematic error described above, but can be reproduced with the Monte Carlo model as demonstrated below and by Burger et al. (2012).

3. Modeling UVVS limb scans

To simulate the UVVS observations of exospheric Ca and determine the size, source rate, and energy distribution of the Ca source on the surface, we used the model of Burger et al. (2010). The model is necessary for correct interpretation of the data because an empirical analysis such as that

presented above cannot correctly take into account variations in observing geometry among orbits and the range in radial velocities relative to the Sun of Ca atoms near Mercury. Descriptions of our model are given by Burger et al. (2010, 2012). For this work we used a constant step-size integrator rather than the variable step-size integrator used by Burger et al. (2010, 2012). This change substantially sped up the simulations with minimal loss of precision ($\lesssim$50 km over the ionization lifetime of a Ca atom) in the regions of the exosphere observed by the dayside limb scans.

Because we found no evidence of year-to-year variability in the data, we grouped the limb scan data into bins of width 5° in Mercury true anomaly. In general, this binning increased the local time coverage and radial sampling of the exosphere as orbits from different years obtained limbscans at different local times and with different radial sampling. The photoionization lifetime and radial velocity of Mercury relative to the Sun are approximately constant over the 5° of true anomaly spanned by each bin. Figure 5 summarizes the number of MESSENGER orbits that contributed data to each bin and the local time coverage as a function of Mercury true anomaly. The number of local times sampled was determined by calculating the local time of the tangent point for each spectral scan and rounding to the nearest hour. (Model simulations used the actual UVVS lines of sight. The rounding was used only to quantify the coverage). Owing to spacecraft viewing restrictions between TAA=180° and TAA=205°, it was not possible to sample local times near noon, and only dawn (6 h local time) and dusk (18 h local time) were measured during the limb scans. Although this limitation made it difficult to determine the width of the source during these times, we do have a measure-

ment of the dawn-to-dusk ratios. "Complete" dayside coverage was achieved for true anomalies with data at 13 distinct local times.

We used the Monte Carlo model to quantify the variations in source rate, size, and temperature by performing a grid search over these three parameters and determining the minimum of the χ^2 statistic. The source was parameterized in the manner of Burger et al. (2012) as a source centered at the dawn equatorial point that falls off exponentially with angle with e-folding width σ:

$$\mathbf{r} = (x, y, z) = (\cos\lambda\cos\mu, \sin\lambda\cos\mu, \sin\mu) \quad (3)$$

$$\cos\phi = \mathbf{r}\cdot\mathbf{r_0} \quad (4)$$

$$f(\lambda,\mu) = f_0 e^{-\phi(\lambda,\mu)/\sigma} \quad (5)$$

where λ and μ are the longitude and latitude relative to the sub-solar point, $f(\lambda,\mu)$ is the flux from the surface as a function of longitude and latitude, f_0 is the maximum flux, and ϕ is the angle defined by a point on the surface, the center of Mercury, and the center of the source ($\mathbf{r_0}$) which we held fixed at the dawn equatorial point ($\lambda = 270°$, $\mu = 0°$). σ is the angular e-folding width of the source. We initially used Maxwellian speed distributions. Although the source may not be thermal, these distributions were indicative of the mean energy of the source and informed our choices of speed distributions in subsequent analyses.

With the results of Burger et al. (2012) as a starting point, we chose temperatures between 2×10^4 K and 7×10^4 K and angular widths between 20° and 80° for our grid search. We also included models with constant Ca flux over the surface (the "isotropic" case) for comparison. At each grid point,

we simulated the emission along each line of sight under the assumption of a nominal source flux from the surface (10^{23} Ca atoms s^{-1}).

To determine the best fit to the data, we computed the standard χ^2 statistic for the models at each grid point. We then found the minimum χ^2 with the fit parameters T, σ, and S, where S is the total source rate in units of 10^{23} atoms s^{-1}. The uncertainties in each fit parameter were determined by varying each parameter separately from the best-fit values and finding the point at which $\Delta\chi^2 = \chi^2_\nu - \chi^2_{\nu,min} = 3.53$, where χ_ν is the reduced χ^2 (χ^2 divided by the number of degrees of freedom, i.e., the number of data points minus the number of fit parameters). $\Delta\chi^2 = 3.53$ gives the one-standard deviation (68.27%) confidence level for a three-parameter fit (Press et al., 2007, p. 815).

The results from the grid search analysis are presented in Figure 6. The temperature is not well constrained, although the source is clearly hot, with a mean temperature $\sim (6 \pm 1) \times 10^4$ K. The upper bound on the temperature is especially difficult to determine because the e-folding distance changes slowly with T for these high temperatures. Essentially, a 60,000 K exosphere looks the same as an 80,000 K exosphere because the calcium is largely escaping. It is also difficult to constrain the variability in the source width precisely. However, σ is consistently between $\sim 40°$ and 80° and may be wider near aphelion than perihelion. Unfortunately, near aphelion the local time coverage was poor, and the data are consistent with both a 60° source and an isotropic source, implying that we have not constrained σ well at these true anomalies. During true anomalies with better local time coverage, σ is between 40° and 60°. In contrast, we do a much better job of constraining

the total source rate. The source rate shows an order of magnitude variation peaking at $3.7 \pm 0.6 \times 10^{23}$ s^{-1} at 20° true anomaly and falling to $0.4 \pm 0.3 \times 10^{23}$ s^{-1} at TAA=195°, almost half an orbit away. The small enhancement in source rate at TAA=165° is associated with an increase in the model uncertainty such that the enhancement is not statistically significant.

The grid search results in Fig. 6a and 6b suggest that the observed exosphere may be consistent with a constant source size and temperature. A test of this hypothesis is shown in Fig. 7, which compares the best-fit results from Fig. 6 with a model in which (T,σ)=(70,000 K, 50°) at all true anomalies. Panel (a) indicates that the total source rate is unaffected by the use of a constant source. Panel (b) shows the difference in χ^2_ν between the models used to make the curves in (a). This comparison indicates that the constant-source model (i.e., constant in temperature and size on the surface, but not in strength) provides a slightly worse fit to the data but within 1 standard deviation uncertainty. Therefore, we conclude that we are unable to identify changes in the temperature and in the size of the Ca source in the dawn region.

The source rates found here are approximately consistent with those found by Burger et al. (2012) (shown in red in Fig. 6c). However, there are several key differences between the earlier and current results that may make a direct comparison inappropriate. First, Burger et al. (2012) made only a limited effort at constraining the temperature; they preferred T=50,000 K but found that for most of the data T=20,000 K worked equally well. The Burger et al. (2012) results shown in Fig. 6 are under the assumption that T=50,000 K, whereas here we have used temperature as a fit parameter.

Second, Burger et al. (2012) found a smaller source width; all the data were well fit with $\sigma \sim 25°$. This result may be because the data used by Burger et al. (2012) were largely over Mercury's nightside, whereas here we have used only dayside measurements. The discrepancy in source width may indicate that the source is asymmetric across the terminator. In this work, we have assumed symmetry (i.e., as much Ca is ejected over the nightside as the dayside), although the current dataset was not sensitive to emission over the nightside. Joint analysis of dayside and nightside data is required to understand any asymmetry across the terminator. Simulations of the dayside limb scans with the nightside Ca source shut off (i.e., no calcium was produced before local time 6 h or after local time 18 h) do not markedly affect the quality of the fits. The limb scan data are thus consistent with no calcium release on the nightside. The data modeled by Burger et al. (2012), however, did require the ejection of Ca from the nightside.

The preceding analysis was based on the assumption that calcium is ejected from the surface with a Maxwellian flux distribution. This assumption may not be valid; potential source processes such as ion sputtering or molecular dissociation can result in non-thermal initial speed distributions. If atomic Ca is produced from the dissociation of Ca-bearing molecules near the surface, the initial speed distribution will be approximately Gaussian in the form:

$$f_v = e^{-(v-v_p)^2/2\eta^2} \tag{6}$$

where v_p is the most probable speed and η is the width of the distribution. To test whether the data are consistent with an initial speed distribution of this form, we conducted a grid search over the parameters v_p, σ, and S,

holding η fixed at 0.2 km s^{-1}. We found that the dayside limb scan data are consistent with this speed distribution for v_p greater than Mercury's escape speed (4.1 km s^{-1}). It was not possible to constrain better the source speed using only these data; the shape of the exosphere is insensitive to the initial speed for escaping atoms. UVVS observations of the nightside or at higher altitudes on the dayside may help to improve definition of the initial speed, but the analysis of those data is beyond the scope of this work.

4. Discussion

We have presented models and analysis of MESSENGER UVVS observations of calcium in Mercury's dayside exosphere. We have found three primary characteristics of the Ca distribution:

- There is a persistent source located in the dawn equatorial region that is approximately constant in size and energy. The source is energetic, consisting of Ca ejected at speeds greater than Mercury's escape velocity. There is no evidence for a colder component to the Ca exosphere.

- There is a clear seasonal variation in the Ca source, with the source rate peaking at 3.7×10^{23} s^{-1} at $\sim 20^{\circ}$ true anomaly and reaching a minimum of 0.4×10^{23} s^{-1} at $\sim 195^{\circ}$ true anomaly.

- There is no evidence of year-to-year variability in the near-surface dayside Ca exosphere.

These results are consistent with ground-based observations indicating high-temperature calcium (Bida et al., 2000; Killen et al., 2005) as well as previous results from MESSENGER UVVS observations (Killen et al., 2010; Burger

et al., 2012) that focused on data over Mercury's nightside. The amount of calcium in the exosphere is extremely low (Fig. 8). Over the course of a Mercury year, the peak density varies from less than 1 cm^{-3} to $\sim$ 4 cm^{-3}, and the total Ca mass varies from $\sim$7 kg to 36 kg. Fig. 8a shows the Ca density in Mercury's equatorial plane at Mercury true anomaly 20° based on our best-fit model to the dayside limbscans; Fig. 8b gives the total number and mass of exospheric Ca atoms. The Ca source rate varies by a factor of 10, whereas the content varies only by a factor of 5 due to the changing Ca photoionization lifetime (the lifetime varies from 23 minutes at perihelion to 52 minutes at aphelion). Near aphelion where the source rate is the lowest, the Ca lifetime is greatest so that the Ca residence time in the exosphere is the longest. The vast majority of the ejected Ca is ionized near Mercury's surface: the fraction of Ca that is photoionized varies between $\sim$80% and 95% over the course of a Mercury year. A smaller fraction, between 3% and 15%, escapes beyond 15 R_M, although that Ca is eventually photoionized. The remainder, $\sim$1–2%, returns to the surface.

Burger et al. (2012) presented several hypotheses for the production of energetic calcium from the dawn region, but they found none consistent with the data they presented. Here we discuss these hypotheses and evaluate them in light of the current results.

Many authors have looked at impact vaporization as a potential exospheric source (e.g., Cintala, 1992; Borin et al., 2009; Grotheer and Livi, 2014). Kameda et al. (2009) and Wang and Ip (2011) argued that the exospheric Na density is correlated with the interplanetary dust (IPD) density at Mercury. This hypothesis has several features that make it a promising sce-

nario for explaining the observed Ca source. First, Ca-bearing molecules are more likely to be produced in impact vapor plumes than Ca atoms (Berezhnoy and Klumov, 2008). These molecules quickly photodissociate (Berezhnoy and Klumov, 2008; Berezhnoy, 2013) to release energetic Ca atoms (Killen et al., 2005). Second, recent observations and models of micrometeoroids at Earth show that there is a strong dawn enhancement in the impactor flux (Janches et al., 2006; Pifko et al., 2013).

Although these arguments are suggestive, several questions must be addressed before we can confidently conclude that micrometeoroid impact vaporization is the primary exospheric Ca source. For example, it has not been demonstrated that the results of Janches et al. (2006) and Pifko et al. (2013) are applicable to Mercury: there are neither measurements nor models of the impactor flux at Mercury's surface as a function of local time. A study of larger meteoroids (radii $\gtrsim$ 1 cm) predicted a leading/trailing asymmetry in the impact flux (Marchi et al., 2005), although that result did not include radiation forces that are important for determining the motions of micrometeoroid impactors. Finally, it is not clear that impact followed by molecular dissociation produces atomic Ca with an effective temperature >50,000 K. However, the molecular species produced in impact vapor plumes and the excess energies of these species upon dissociation are not well understood.

Several authors have suggested mechanisms for producing dawn enhancements in the sodium exosphere through enhancements of sodium on the nightside by enhancing the surface abundance of Na on the nightside by either implanted magnetospheric Na^+ (Sprague et al., 1997) or by thermally driven migration of sodium from the dayside to the nightside (Mura et al., 2009;

Leblanc and Johnson, 2010). We believe it is unlikely that the Ca source is driven by nightside material moving into sunlight. While the data analyzed here are not sensitive to a nightside source, those analyzed by Burger et al. (2012) were. Their results required a Ca source on the nightside of the terminator, which is inconsistent with mechanisms requiring sunlight. In addition, between Mercury true anomaly 335° and 25°, inclusive of perihelion, the motion of the Sun in the sky reverses so that new material is not being brought into sunlight. However, this is when the Ca source rate is greatest – the peak source rate is at TAA=20°, and the source rate is above the mean value of 1.6×10^{23} during this entire period. At this true anomaly, the regolith near the terminator has already been in sunlight and returned to the terminator region. If material which had accumulated on the nightside were being degassed, we one might expect the source rate to be minimized at this time. However, additional modeling of the state of calcium on the surface and the physical mechanisms by which it is vaporized or desorbed is required to determine when the seasonal peak in the calcium source should occur.

Finally, the interaction between Mercury's magnetosphere and the solar wind might contribute to the production of exospheric calcium. Precipitation of solar wind ions onto the surface is thought to affect the flux of sodium from the surface due to direct ion sputtering (McGrath et al., 1986), chemical sputtering (Potter, 1995; Mura et al., 2009), or ion-enhanced diffusion of sodium followed by photon-stimulated desorption (Sarantos et al., 2010; Burger et al., 2010). Ion precipitation has generally been associated with spots of high-latitude Na emission seen in ground-based data. We see no

evidence for similar high-latitude Ca emission, although the limb scan observations may not be sensitive to the proper regions. Ion precipitation on the nightside might lead to an enhancement of calcium, but as discussed above the mechanism does not appear to involve material rotating into sunlight. There is no evidence of enhanced ion precipitation in the dawn region, so we conclude that ion precipitation is not related to the Ca production. In general, magnetospheric interaction effects such as ion sputtering or electron-stimulated desorption are unlikely to be the primary Ca source mechanism because of the intrinsic variability of the magnetosphere compared with the regularly varying Ca source rate.

To summarize, we have used MESSENGER data to identify a seasonal dependence to the dawn source of Mercury's dayside exospheric calcium. The mechanism responsible for ejecting calcium from the surface is not determined, but molecular dissociation of Ca-bearing molecules produced in micrometeoroid impact vapor appears to be most consistent with these results. Future work that focuses on joint modeling of dayside and nightside data to better constrain the size and variability of the source region is warranted as a step toward a better understanding of the physical mechanism responsible for its production.

References

Berezhnoy, A.A., 2013. Chemistry of impact events on the Moon. Icarus 226, 205–211, doi:10.1016/j.icarus.2013.05.030.

Berezhnoy, A.A., Klumov, B.A., 2008. Impacts as sources of the exosphere on Mercury. Icarus 195, 511–522, doi:10.1016/j.icarus.2008.01.005.

Bida, T.A., Killen, R.M., Morgan, T.H., 2000. Discovery of calcium in Mercury's atmosphere. Nature 404, 159–161.

Borin, P., Cremonese, G., Marzari, F., Bruno, M., Marchi, S. 2009. Statistical analysis of micrometeoroids flux on Mercury. Astron. Astrophys. 503, 259–264.

Burger, M.H., Killen, R.M., Vervack, Jr., R.J., Bradley, E.T., McClintock, W.E., Sarantos, M., Benna, M., Mouawad, N. 2010. Monte Carlo modeling of sodium in Mercury's exosphere during the first two MESSENGER flybys. Icarus 209, 63–74, doi:10.1016/j.icarus.2010.05.007.

Burger, M.H., Killen, R.M., McClintock, W.E., Vervack, Jr., R.J., Merkel, A.W., Sprague, A.L., Sarantos, M. 2012. Modeling MESSENGER observations of calcium in Mercury's exosphere. J. Geophys. Res. 117, E00L11, doi:10.1029/2012JE004158.

Chamberlain, J.W., 1963. Planetary coronae and atmospheric evaporation. Planet. Space Sci. 11, 901–960.

Cintala, M.J., 1992. Impact-induced thermal effects in the lunar and Mercurian regoliths. J. Geophys. Res. 97, 947–973.

Grotheer, E.B., Livi, S.A. 2014. Small meteoroids' major contribution to Mercury's exosphere. Icarus 227, 1–7, doi:10.1016/j.icarus.2013.07.032.

Janches, D., Heinselman, C.J., Chau, J.L., Chandran, A., Woodman, R., 2006. Modeling the global micrometeor input function in the upper atmosphere observed by high power and large aperture radars. J. Geophys. Res. 111, A07317, doi:10.1029/2006JA011628.

Kameda, S., Yoshikawa, I, Kagitani, M, Okano, S. 2009. Interplanetary dust distribution and temporal variability of Mercury's atmospheric Na. Geophys. Res. Lett. 36, L15201, doi:10.1029/2009GL039036.

Killen, R.M., Bida, T.A., Morgan, T.H. 2005. The calcium exosphere of Mercury. Icarus 173, 300–311, doi:10.1016/j.icarus.2004.08.022.

Killen, R.M., et al., 2007. Processes that promote and deplete the exosphere of Mercury. Space Sci. Rev. 132, 433–509.

Killen, R.M., Shemansky, D., Mouawad, N., 2009. Expected emission from Mercury's exospheric species, and their ultraviolet-visible signatures. Astrophys. J. Supp. Ser. 181, 351–359.

Killen, R.M., Potter, A.E., Vervack, Jr., R.J., Bradley, E.T., McClintock, W.E., Anderson, C.M., Burger, M.H. 2009. Observations of metallic species in Mercury's exosphere. Icarus 209, 75–87, doi:10.1016/j.icarus.2010.02.018.

Leblanc, F., Johnson, R.E. 2010. Mercury exosphere I. Global circulation model of its sodium component. Icarus 209, 280–300, doi:10.1016/j.icarus.2010.04.020.

Marchi, S., Morbidelli, A., Cremonese, G. 2005. Flux of meteoroid impacts on Mercury. Astron. and Astrophys. 431, 1123–1127, doi:10.1051/0004-6361:20041800

McClintock, W.E., Lankton, M.R., 2007. The Mercury Atmospheric and Surface Composition Spectrometer for the MESSENGER mission. Space Sci. Rev. 131, 481–521.

McClintock, W.E., Bradley, E.T., Vervack, Jr., R.J., Killen, R.M., Sprague, A.L., Izenberg, N.R., Solomon, S.C., 2008. Mercury's exosphere: Observations during MESSENGER's first Mercury flyby. Science 321, 92–94.

McGrath, M.A., Johnson, R.E., Lanzerotti, L.J., 1986. Sputtering of sodium on the planet Mercury. Nature 323, 694–696.

Mura, A., Wurz, P., Lichtenegger, H.I.M., Schleicher, H., Lammer, H., Delcourt, D., Milillo, A., Orsini, S., Massetti, S., Khodachenko, M.L., 2009. The sodium exosphere of Mercury: Comparison between observations during Mercury's transit and model results. Icarus 200, 1–11.

Pifko, S., Janches, D., Close, S., Sparks, J., Nakamura, T., Nesvorny, D., 2013. The Meteoroid Input Function and predictions of mid-latitude meteor observations by the MU radar. Icarus 223, 444–459, doi:10.1016/j.icarus.2012.12.014.

Potter, A.E. 1995. Chemical sputtering could produce sodium vapor and ice on Mercury. Geophys. Res. Lett. 22, 3289–3292.

Press, W.H., Teukolsky, S.A., Vetterling, W.T., Flannery, B.P., 2007. Numerical Recipes: The Art of Scientific Computing, 3rd ed., Cambridge Univ. Press, Cambridge, 1235 pp.

Sarantos, M., Killen, R.M., Sharma, A.S., Slavin, J.A., 2010. Sources of sodium in the lunar exosphere: Modeling using ground-based observations and spacecraft data of the plasma. Icarus 205, 364–374, doi:10.1016/j.icarus.2009.07.039.

Sprague, A.L., Kozlowski, R.W.H., Hunten, D.M., Schneider, N.M., Domingue, D.L., Wells, W.K., Schmitt, W., Fink, U., 1997. Distribution and abundance of sodium in Mercury's atmosphere. 1985–1988. Icarus 129, 506–527.

Wang, Y.-C., Ip, W.-H., 2011. Source dependency of exospheric sodium on Mercury. Icarus 216, 387–402, doi:10.1016/j.icarus.2011.09.023.

Table 1: Summary of dayside limb scans

Number of Limb Scans per Orbit	**Number of Orbits**
1	21
2	98
3	37
4	120
5	71
6	26
7	62
8	16
9	9
10	2
11	1
12	0
13	2
Total	**465**

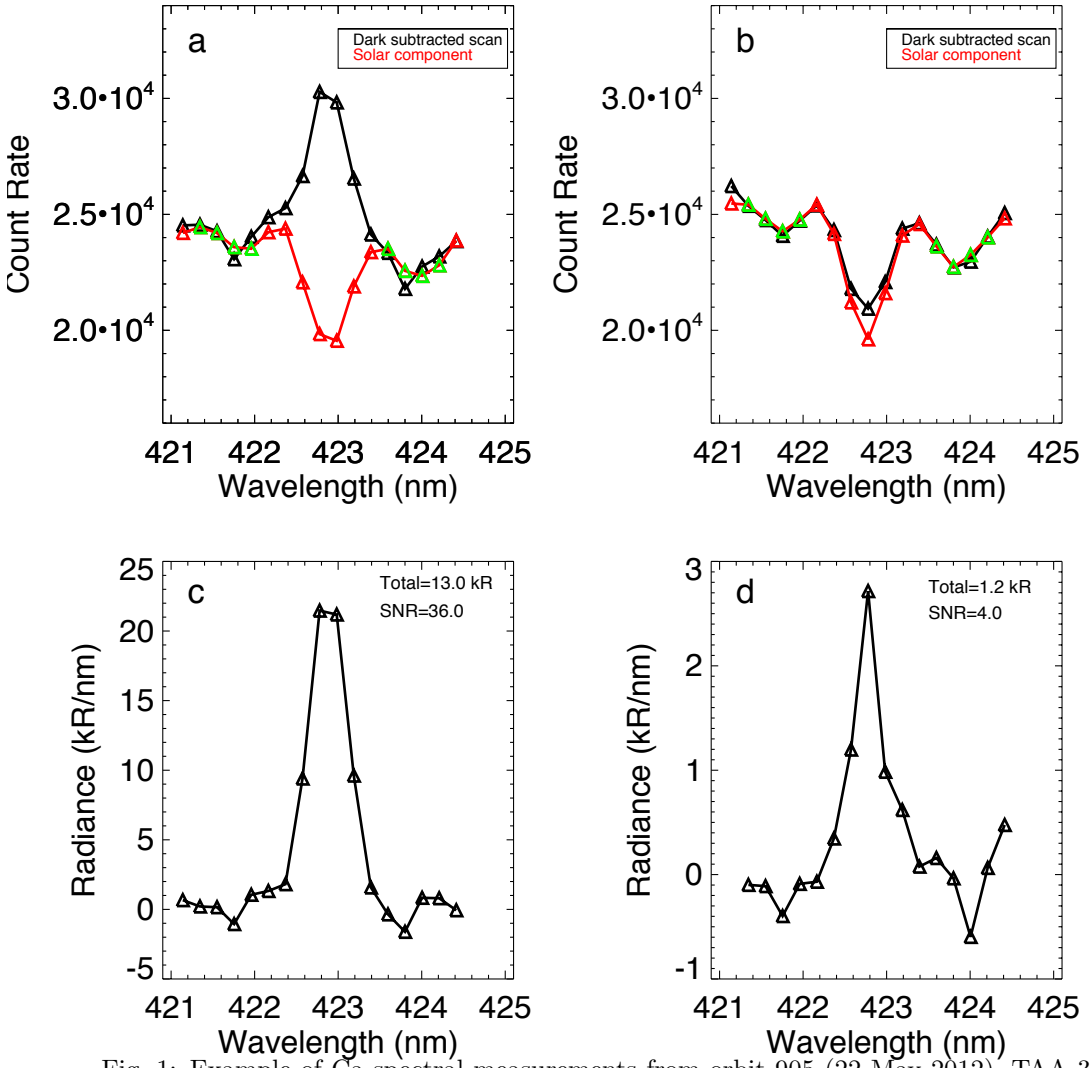

Fig. 1: Example of Ca spectral measurements from orbit 905 (22 May 2012), TAA 316°, tangent altitude near 220 km. (a) The scan was taken near the dawn terminator where there is an abundance of Ca. The spectral scan with dark count rate subtracted is represented in black. The fitted solar spectral component is in red. The points used to fit the solar spectrum are in green. (b) Same as (a) but taken near the dusk terminator where the abundance of Ca is small. (c) Resulting radiance value from (a). (d) Resulting radiance value from (b).

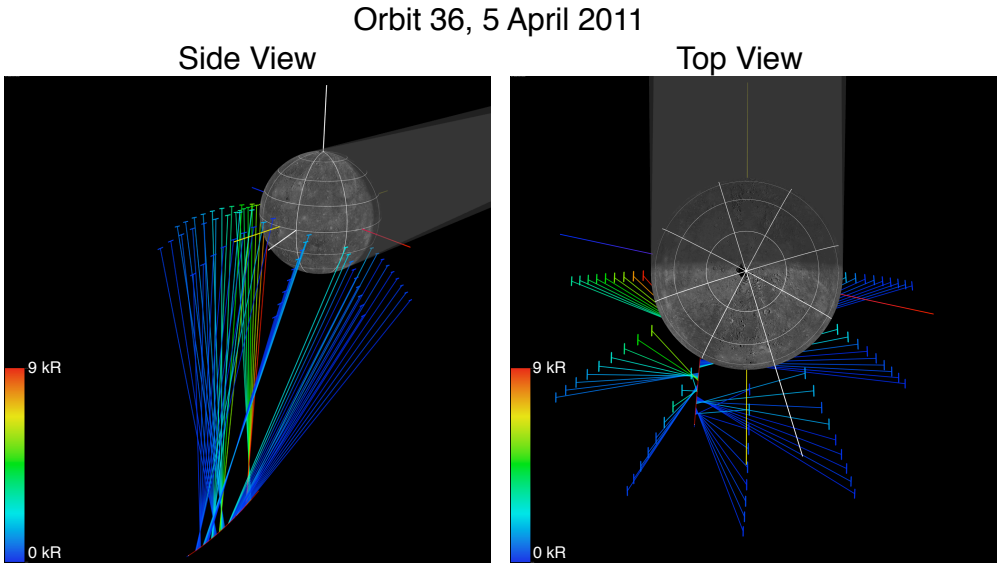

Fig. 2: Two views of limb scan observations over Mercury's dayside from 5 April 2011. The anti-Sunward direction is indicated by Mercury's shadow (the grey shaded region). The lines of sight extend from the spacecraft orbit (indicated by the red line) to the line-of-sight tangent point.

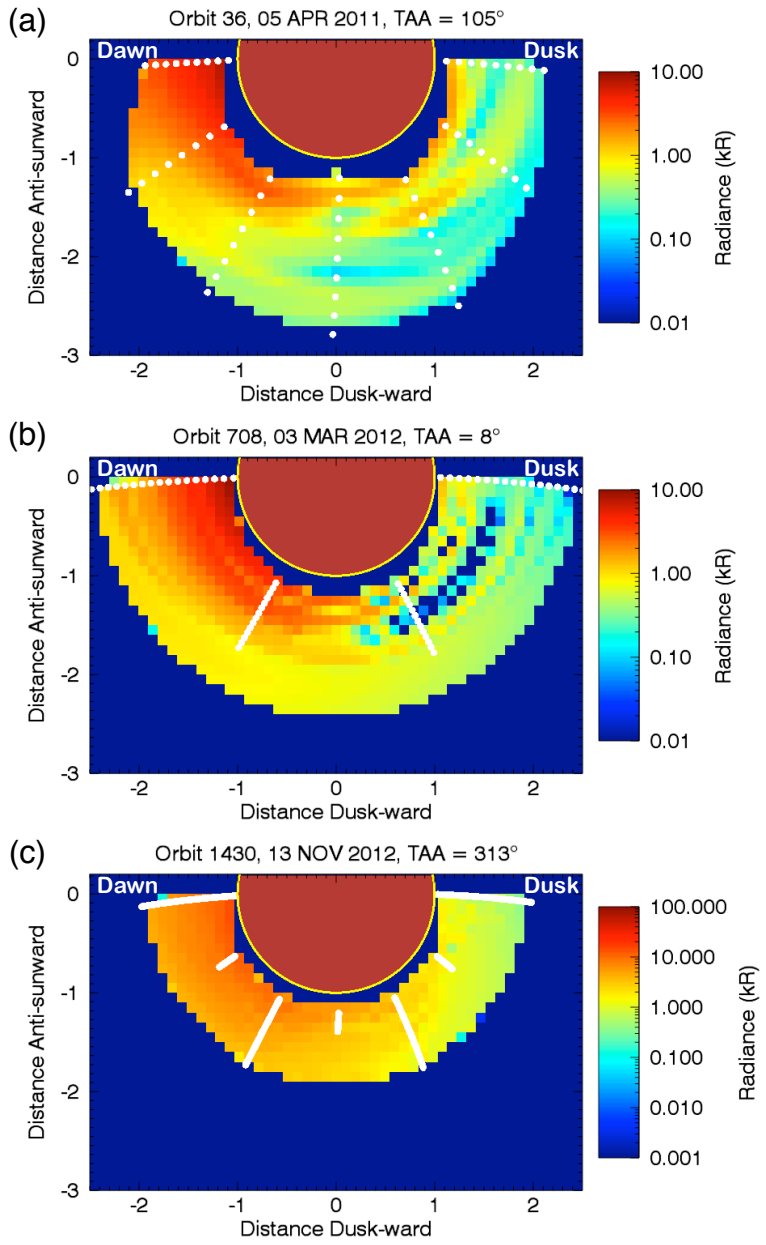

Fig. 3: Reconstructed images of Ca emission in Mercury's dayside equatorial plane at three epochs. The white circles show the projections of the line-of-sight tangent points in the equatorial plane. The color scale indicates the interpolated radiance. Mercury's sunlit hemisphere is shown. The dawn terminator is at the left side of the disk; the sub-solar point is at the bottom. The lines of sight for the observation in (a) are shown in Fig. 2.

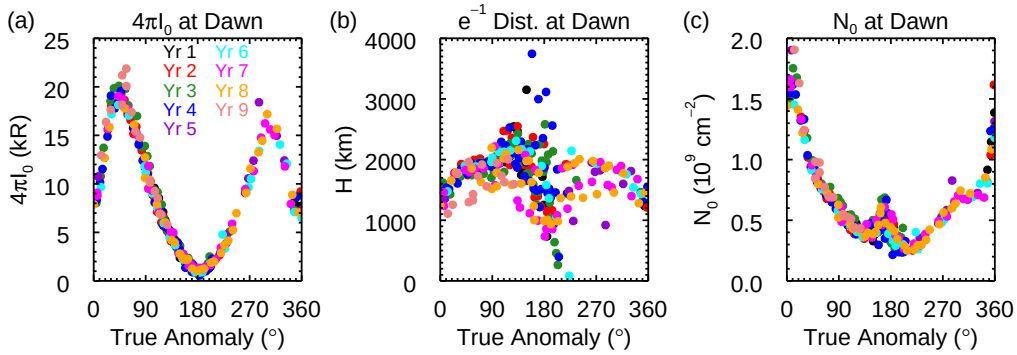

Fig. 4: (a) Intensity at the surface over Mercury dawn determined from exponential fits to radial limb scan data. Different Mercury years are indicated by different colors. (b) The e-folding distance over dawn determined from the exponential fits. (c) Apparent tangent column density over dawn. A systematic error that enhances the peak at perihelion and creates the apparent peak near aphelion has been introduced by the assumption that all the atoms are at rest relative to Mercury (see text).

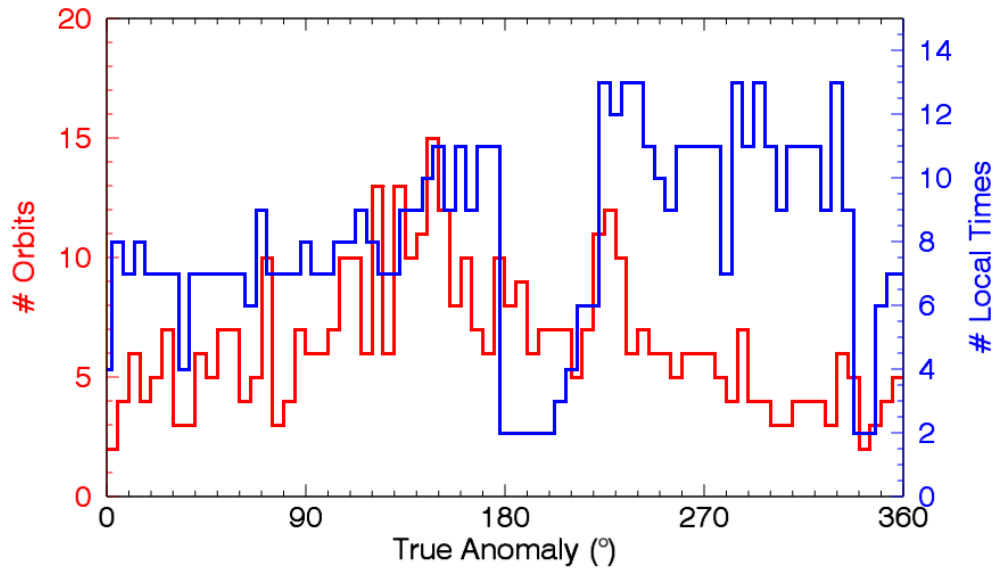

Fig. 5: Number of orbits (red) and number of distinct local times above the surface sampled (blue) in each 5° true anomaly bin as a function of true anomaly.

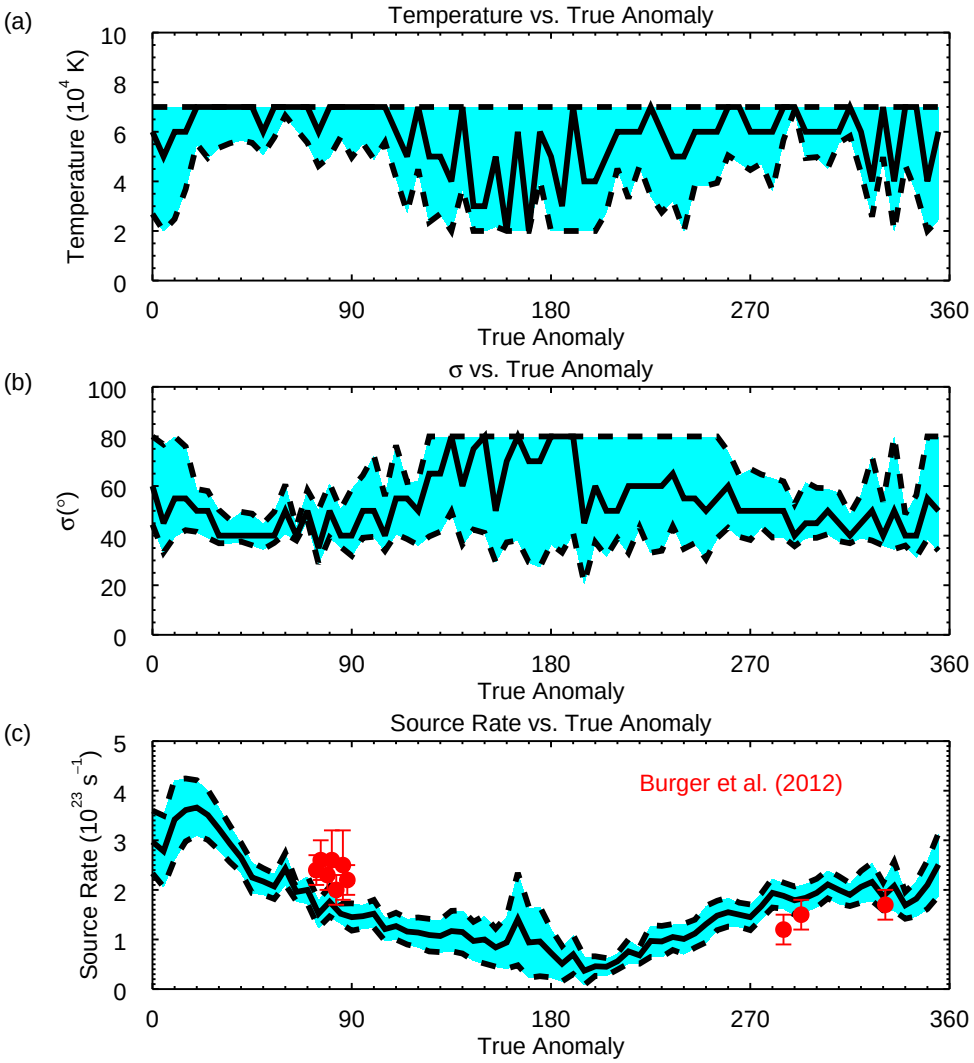

Fig. 6: Best-fit parameters to the dayside limb data under the assumption of a maxwellian speed distribution and a source region centered on the dawn equatorial point as a function of true anomaly. The best fits are given by the solid lines with the one standard deviation uncertainties indicated by the shaded region between the broken lines. (a) Fit to source temperature. The temperature was constrained by the grid search parameters to be between 20,000 K and 70,000 K. (b) Fit to source width. The width was constrained between 20° and 80°. (c) Fit to source strength. There were no constraints on the source rate. The source rates determined by Burger et al. (2012) are shown in red.

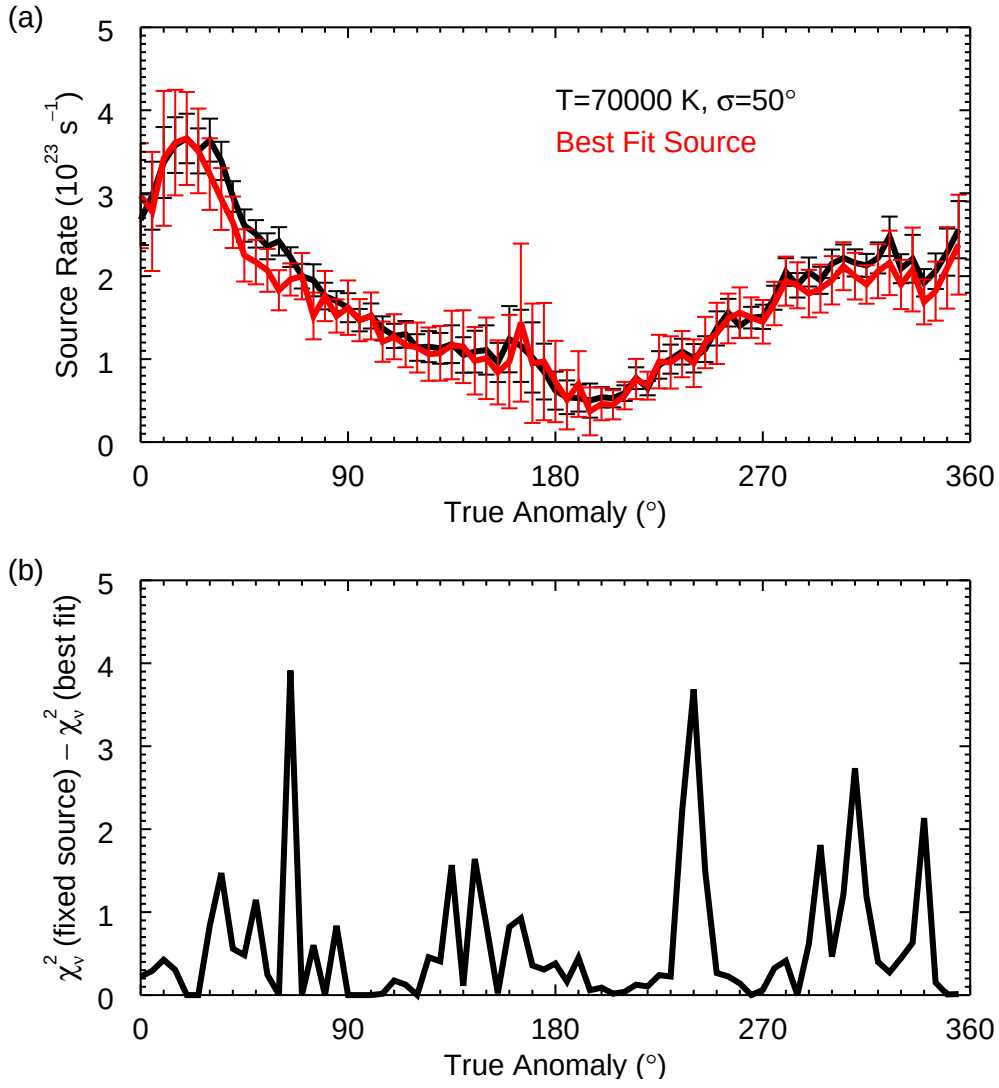

Fig. 7: (a) Comparison of the best-fit source rate shown in Fig. 6c (red) and the source rate determined using a source with T=70,000 K and σ=50° at all true anomalies. (b) Difference in χ^2_ν between the constant source shown in (a) and the best-fit (i.e., minimum) value.

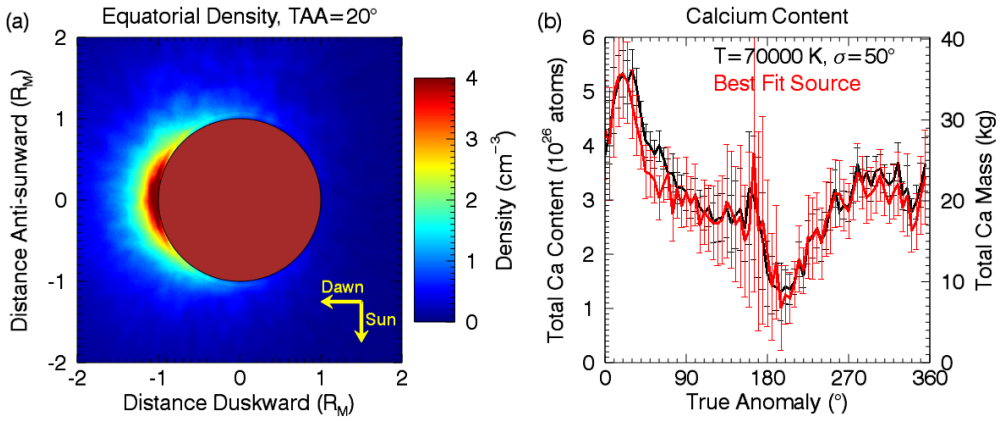

Fig. 8: (a) Ca density in Mercury's equatorial plane at Mercury true anomaly=20° based on our best-fit model (T=70,000 K, σ=50°, S=3.7 × 10^{23} s^{-1}). (b) Modeled calcium content given in terms of total number of Ca atoms in the exosphere and total Ca mass as a function of Mercury true anomaly. The red line shows the density for our best-fit models; the black line denotes a source with a fixed temperature and width as indicated.